Modified copper zinc ferrite nanoparticles doped with Zr ions for hyperthermia applications

B. I. Salem[1] · O. M. Hemeda[1] · A. M. A. Henaish[1,2] · N. Y. Mostafa[3] · M. Mostafa[1]

Abstract

The problem of the present work is to synthesize a nanomagnetic material with low T_C below 45 °C and its particle size below 30 nm to be appropriate material for convert magnetic loss into heat energy. A series of $Cu_{0.4}Zn_{0.6+y}Zr_yFe_{2-2y}O_4$ nanoparticles compositions where $y = (0.05, 0.1)$ were synthesized via citrate sol–gel method. The prepared samples were characterized by X-ray diffraction (XRD) and transmission electron microscopy (TEM). The grains were observed from SEM confirming the crystalline structure of the ferrite which was detected by X-ray diffraction. Magnetic hysteresis loop measurements illustrate that materials exhibit soft magnetic properties at low Zr content, while at higher Zr content all materials behave as superparamagnetically without any saturation magnetization M_s. The initial magnetic permeability (μ_i) at frequency 10 kHz as a function of temperature was measured. A sudden change in μ_i appears around Curie temperature, making our samples good candidates for magnetic temperature transducer (MTT) devices. The DC resistivity for sample at $y = 0.05, 0.1$ was studied. The resistivity decreases linearly with increasing temperature within the given range of temperature up to 666 K for all samples. The dielectric constant of all samples is nearly independent on temperature through the range of 450 to 600 K which is a common character of ferrites. The dielectric loss was found to increase by increasing temperature, which may be related to the increase in AC conductivity. Hyperthermia measurements show the maximum specific power loss and temperature increase were 26 w/gr and 43 °C, respectively, for sample containing Zr = 0.05, after 2 min of measurements. One of the real applications of the material is that it is used as an effective method in tumor treatment by exposing the patient to external magnetic field.

Keywords Citrate sol–gel method · Permeability · DC resistivity · Hysteresis loop · Hyperthermia

1 Introduction:

Due to enhanced properties of nanoparticles (NPs) compared with counterpart bulk materials, they have been used widely in modern fields of technology [1, 2]. One type of NPs which is called spinel ferrites with the general formula AFe_2O_4 (A = Mn, Co, Ni, Mg, or Zn) is unique due to their tunable physical and chemical properties according to their nanoscale size [3]. They also can be produced in many forms, such as thin films [4] and nanopowders [5] that can be shaped as nanofibers [6], nanowires [7], nanospheres [8], and any desired geometry particles [9]. Applications of spinel ferrites NPs include biosensor [10], photocatalysis [11], drug delivery [12], and hyperthermia [13].

Salavati-Niasari et al. prepared Mn_3O_4 nanoparticles using the thermal decomposition method, and their physicochemical characterization was done. The Mn_3O_4 obtained has been characterized using SEM, TEM, XRD, XPS, and FTIR. The particles were mostly tetragonal Mn_3O_4 phase and had a size in the range 20–30 nm. Significantly, the metallic impurities were below 0.01%, and so high-quality products were prepared [14]. A new catalytic method for the selective benzylation of benzene to diphenylmethane using alumina-supported metal chloride as the catalyst and benzyl chloride as the benzylating agent has been studied. The simple preparation, low cost, and easy handling of this catalyst prompted us to study its application for benzylation, an

✉ B. I. Salem
basant.salem@science.tanta.edu.eg

1 Physics Department, Faculty of Science, Tanta University, Tanta, Egypt

2 NANOTECH Center, Ural Federal University, 620002 Yekaterinburg, Russia

3 Chemistry Department, Faculty of Science, Suez Canal University, Ismailia 41522, Egypt

important reaction for the diphenylmethane synthesis [15]. Pure holmium oxide ceramic nanostructures were prepared via a new simple approach. The structural and optical properties of the as-prepared nanostructures were characterized by techniques such as FESEM, TEM, FTIR, XRD, UV–Vis diffuse reflectance spectroscopy, and EDS. The obtained holmium oxide nanostructures can be utilized as an interesting candidate for photocatalytic applications under UV light such as removal of rhodamine B as cationic dye [16]. Flower-like magnesium hydroxide (Mg (OH)$_2$) nanostructures were synthesized used the hydrothermal process. The effect of Mg (OH)$_2$ nanostructures on the thermal stability of the polymeric matrixes has been investigated. Mg (OH)$_2$ has also barrier effect to slow down the product volatilization and thermal transport during decomposition of the polymers [17]. Star-shaped PbS nanoparticles were synthesized using two methods: thermal decomposition and hydrothermal route. The use of thiosemicarbazide (TSC) complexes of different structures as new precursor allows controlling the structure of obtained semiconductor materials. In this paper, a simple, green, low cost, and reproducible process for the synthesis of PbS nanocrystals is reported [18]. A novel synthetic strategy for preparation of ZnS(Pn)$_{0.5}$ nanotubes with Zn(Pn)$_2$ as a Zn^{2+} source and thioglycolic acid (TGA) as a sulfur source and stabilizing agent in aqueous solution at relatively low temperature (75°C) was made. The effect of TGA concentration on morphology of the as-prepared products was studied. Then, they investigated conversion of ZnS(Pn)$_{0.5}$ nanotubes to ZnS and ZnO nanostructures and finally survey optical properties of as-obtained products [19]. The Fe$_2$O$_3$/CuFe$_2$O$_4$/chitosan nanocomposites have been successfully synthesized via a new sol–gel auto-combustion route. Chitosan was used to functionalize and modify the ferrite nanostructures and also to improve surface properties. The nanocomposites were also characterized by several techniques including SEM, TEM, XRD, IR, and VSM. The effects of amount of onion and chitosan on nanocomposites are to enhance loading capacity when used in magnetic targeted delivery and metal ions adsorption. This approach is simple, low cost, and friendly to the environment. [20]. A simple and environmentally friendly route to develop nanostructures (Dy$_2$Sn$_2$O$_7$) with the aid of Ficus carica extract as naturally available fuel was descried, for the first time which illustrates a great efficiency to destruct target pollutants [21].

Reza Eivazzadeh-Keihan et al. designed a new nanobiocomposite scaffold which is presented by incorporation of carboxymethyl cellulose hydrogels. Biological evaluation of the CMC hydrogel/SF/Mg(OH)$_2$ nanobiocomposite scaffold was conducted via in vitro cell viability assays and in vivo assays, red blood cell hemolysis, and antibiofilm assays. From the results, the CMC hydrogel/SF/Mg(OH)$_2$ nanobiocomposite could be considered a new candidate for further

investigation in other biomedical fields like tissue engineering [22]. A new magnetic nanocomposite (CuFe$_2$O$_4$ MNPs) with a statistical star polymer structure was designed and synthesized. Magnetic nanostructure confirmed the formation of polyamide chains. The obtained images from SEM imaging showed a unique nanoflower morphology which was the proper orientation results of synthesized nanoplates. Finally, the magnetic nanostructure showed a good potential for hyperthermia applications [23]. A new cross-linked lignin–agarose/SF/ZnCr$_2$O$_4$ nanobiocomposite scaffold is designed and introduced. FTIR, EDX, FESEM, and TG analyses as well as mechanical tensile experiments were applied to characterize the structural properties of the nanobiocomposite. Then, the cytotoxicity of this nanobiocomposite scaffold was checked. In addition to this, RBC hemolytic and anti-biofilm assays were undertaken to determine its in vitro blood biocompatibility as well as antibacterial activity [24].

Recently, mixed spinel magnetic nanoparticles (MSMNs) have received attraction for application in medicine by addition of transition metals like Cu^{2+} and Zn^{2+} and control over chemical and physical properties of MSMNs which are imperative for biological applications [25]. Several studies evaluated the magnetic and electrical properties of Mg$_{0.5}$Zn$_{0.5}$Fe$_2$O$_4$ by substitution of Mg^{2+} by Cu^{2+} ions [26–28]. However, most of Cu^{2+}-substituted Mg-Zn ferrite nanoparticles were only studied their magnetic and electrical properties, but few attentions have been paid to the applications of these materials from biomedical point of view. In particular, the hyperthermia capability of magnetic nanoparticles, by which they convert dissipated magnetic energy into thermal energy, enables cancer treatment. Such hyperthermia treatment depends on heating of the region affected by cancer, where the temperatures between 43 and 45 °C can be reached using magnetic nanoparticles under an alternating current (AC) magnetic field [29–31]. Hyperthermia (HT) is a process of implantation of the magnetic material in the tumor tissue and is activated by an external magnetic source. The hyperthermia treatment depends on the properties of magnetic material and external magnetic field [32]. Hyperthermia therapy using magnetic materials as nanosized features has been considered as new tool for the tumor treatment, and many recent researches reported the success of these materials and tools [33–38, 43]. The cancer tissues are killed around 43 °C [39], whereas the normal cell does not affect [32]. One of the most disadvantages of hyperthermia is the limitation of this method which is very useful for the local tumor area but not effective for the migrated tumor. Spinel ferrite nanoparticles have great contribution in hyperthermia such as ZnFe$_2$O$_4$, CuFe$_2$O$_4$, and MgFe$_2$O$_4$ [40–42].

Liu et al. prepared a novel Co-doped NiZn ferrites (CNZF) with a stoichiometric formula of Co$_{0.2}$Ni$_{0.4}$Zn$_{0.4}$Fe$_2$O$_4$, which were loaded on the surface

of graphene (GN) sheets by using hydrothermal method. Phase structure, morphology, magnetic and electromagnetic performances of the nanocomposites were studied. It is expected that this CNZF/GN nanocomposite can be used as a new kind of efficient microwave absorbers with lightweight [43]. A two-novel flower-like NiO hierarchical structures, rose-flower (S1) and silk-flower (S2), were synthesized by using a facial hydrothermal method, coupled with subsequent post-annealing process. Structures, morphologies, magnetic and electromagnetic properties of two NiO structures have been systematically investigated. Due to their large surface-to-volume ratio and hierarchical structures, the NiO nanoflowers exhibited strong absorbing performance, which could be considered as a new generation of absorption materials [44]. A novel hierarchical composite of $Co_{0.2}Ni_{0.4}Zn_{0.4}Fe_2O_4$ nanoparticles (CNZF) decorated on MXenes ($Ti_3C_2T_x$/CNZF) was fabricated by a moderate hydrothermal reaction. The dielectric loss and multiple scattering of $Ti_3C_2T_x$/CNZF are greatly enhanced. Accordingly, the composite exhibited a remarkable microwave absorption, with a maximum reflectivity. This provides a strategy to design promising 2D microwave absorbing materials with great absorbing intensity, efficient absorbing bandwidth, and small thickness [45].

It was found that the ideal material for HT application must have the following features:

1. High saturation magnetization and large area under hysteresis loop, which give high magnetic loss that transfers to heat. The best material that releases sufficient heat at low frequency and external magnetic strength. Another interesting feature is the low Curie temperature around 45 °C, in which material becomes paramagnetic and does not produce any heat above this temperature, and this feature avoids damage to the surrounding tissue.
2. Small particle size.
3. Compatibility and bioactivity, which are very important features for material dealing with HT, because the material must embed in human body by injection and must interact with the body organ.

The aim of this study is to develop nanomagnetic particles with low Curie temperature and a considerable area of hysteresis loop which is capable to produce heat and raise its temperature up to 45 °C to destroy the malignant cell when exposed to external high-frequency magnetic field produced from electromagnet. To achieve this aim of the work, some analyses such as X-ray, FTIR, SEM, permeability, magnetic hysteresis loop, and dielectric properties were studied. In this work, we use $CuZnZrFe_2O_4$ for the first time as a new magnetic material for HT applications and study the effect of Zr content on its hyperthermia properties.

2 Materials and methods

Two samples of $Cu_{0.4}Zn_{0.6+y}Zr_yFe_{2-2y}O_4$ were prepared by sol–gel method and were annealed at 800 °C. In typical procedure, the stoichiometric amounts of cupper nitrate, ferric nitrate, zinc nitrate, and zirconium oxychloride were taken in a glass beaker and dissolved in de-ionized water. The compositions of the Zn and Zr-substituted $CuFe_2O_4$ were represented by $Cu_{0.4}Zn_{0.6+y}Zr_yFe_{2-2y}O_4$ when $y = (0.05,$ and 0.1). The solution was heated on a hot plate up to 60 °C, and then, citric acid was added. The metal nitrates/citric acid molar ratio was fixed at 1:1. The citrate–nitrate mixture was heated and vigorously stirred with magnetic stirrer at 90 °C until a gel was formed. The resulting gel was placed in a drying oven at 105 °C for 24 h. The dried gel was crushed using an agate mortar and transformed into muffle furnace at 800 °C in alumina crucibles [46]. Flowchart for preparation method is shown in Fig. 1.

Calorimetric measurements of the sample were performed using electromagnet with magnetic field 500 Oe at frequency 400 kHz as shown in Fig. 2. Two samples of ferrite were separately placed at the center of the magnet in 300 mL deionized water in quart tube for 16 min. The powder was well dispersed in distilled water using sonicator. Initial and final temperatures were measured using the digital thermometer. The efficiency of heating is defined as specific power loss (SPL) or the power of heating per gm and is given by the equation [47, 48]:

$$SPL = \left(\frac{m}{m_w}\right) C_w \frac{\Delta T}{\Delta t}$$

where m is the mass of magnetic particles $= 2$ g, m_w is the mass of water, c_w is the specific heat capacity of water 4.2 J/g c, and $\frac{\Delta T}{\Delta t}$ is the variation of temperature in defined time Δt.

The samples were examined by X-ray diffraction using a Philips model (PW-1729) diffractometer (Cu-Kα radiation source with $\lambda = 1.540598$ Å) with 2Θ in the range from 4° to 80°. Infrared spectra for the prepared samples were carried out at room temperature by using a Perkin-Elmer-1430 where the recording infrared spectra were in the range 200 to 4000 cm^{-1} (at Tanta University, Central lab.). The microstructure of the samples was analyzed using a scanning electron microscope (SEM) (JEOL JSM-6460, Japan). The DC resistivity is measured by using Electrometer (Keithley 610C). The initial permeability (μ_i) for all toroidal samples is measured as a function of temperature at frequency 10 kHz. The magnetic hysteresis loops were measured at room temperature using vibrating sample magnetometer (VSM) operating system v 1.6 control software Oxford OX8JTL England. RLC Bridge of type BM591 was used for the measurement of the dielectric constant (ε) of the
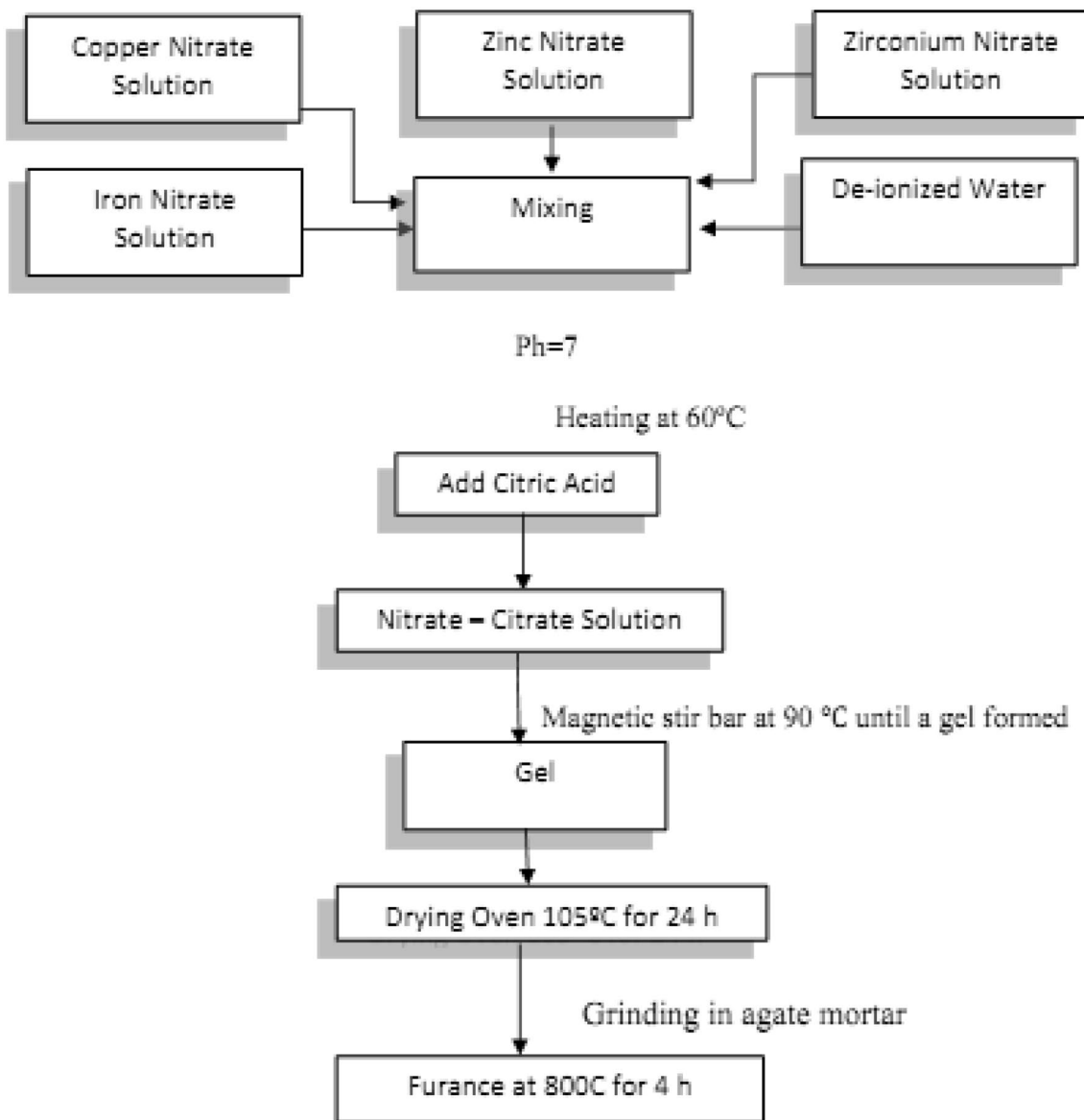
Fig. 1 The citrate sol–gel preparation diagram

prepared samples at different temperatures at two frequencies 1KHZ and 10KHZ.

3 Results and discussion

3.1 X-ray diffraction analysis

Figure 3 shows the X-ray diffraction patterns of $Cu_{0.4}Zn_{0.6+y}Zr_yFe_{2-2y}O_4$ ferrite where (y = 0.05 and 0.1). The formation of the pure spinel phase was confirmed by using XRD. The crystallite size was estimated from the high intensity peaks [(220) (311) (511) (440)] by using Scherer's equation [49, 50]:

$$D = \frac{K\lambda}{\beta \cos \theta}$$

where K is the Scherer's constant equal 0.89. λ is the wavelength of the X-ray for Cu-K_α ($\lambda = 1.5405$Å), θ is the diffraction angle, and β is the full width at half maximum (FWHM) in radian. It is observed that the crystallite size for sample with Zr content ($y = 0.1$) is greater than ($y = 0.05$) as given in Table 1. The lattice parameter was calculated and is given in Table 1. EDS results show that for $y = 0.05$ the atomic weight % of Fe, Cu, Zn, and Zr was (15.47%, 3.14%, 6.42%, 0.24%) and for $y = 0.1$ was (8.88%, 1.76%, 3.80%, 0.48%).
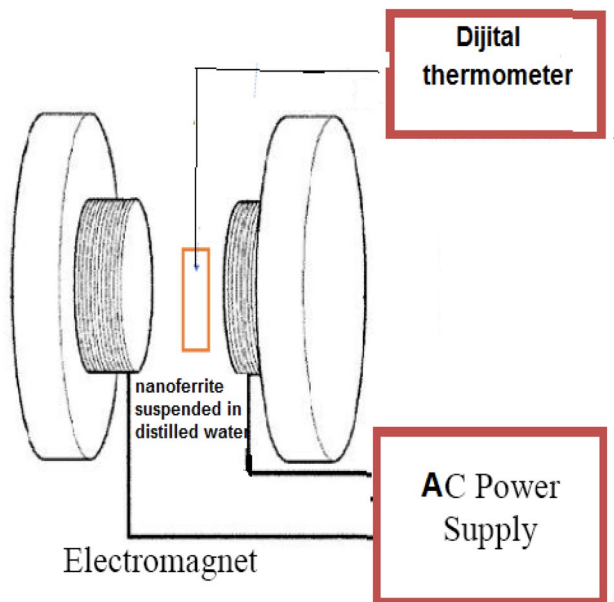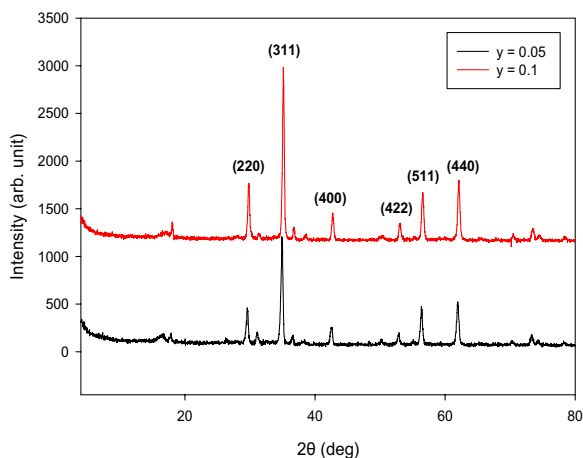
Fig. 2 Setup diagram of HT circuit

Fig. 3 XRD pattern of $Cu_{0.4}Zn_{0.6+y}Zr_yFe_{2-2y}O_4$ ferrite doped with Zr ions with mole content ($y = 0.05$ and 0.1)

Table 1 The structural parameters of (Cu–Zn–Zr) ferrite samples

Y	Lattice parameters a_{exp} (Å)	Particle size D (nm) from X-ray	Grain size from SEM (µm)
0.05	8.5	20.8	3.75
0.1	8.42	27.6	3.19

3.2 Scanning electron microscopy analysis (SEM):

Figure 4 represents the SEM micrograph for $Cu_{0.4}Zn_{0.6+y}Zr_yFe_{2-2y}O_4$ ($y = 0.05$, 0.1). The grains were observed confirming the crystalline nature of the ferrite which was detected by X-ray diffraction as given in Table 1. The values of the grain size for our samples decrease by increasing Zr content as given in Table 1. The accommodations of Zr on the grain boundary inhibit the grain growth. The compositional analysis of our samples was confirmed using energy-dispersive X-ray analysis (EDX) as shown in Fig. 4. The quantitative analysis revealed the relative atomic ratio Fe/Cu/Zn/Zr which is closed to the expected value $Cu_{0.4}Zn_{0.6+y}Zr_yFe_{2-2y}O_4$. The data of EDX analysis are given in Table 1.

3.3 The Fourier transform infrared (FTIR)

The FTIR absorption spectra for $Cu_{0.4}Zn_{0.6+y}Zr_yFe_{2-2y}O_4$ where ($y = 0.05$ and 0.1) are shown in Fig. 5, in the frequency ranges from 200–4000 cm^{-1}. The presence of the two characteristic absorption band υ_1 for tetrahedral site and υ_2 for octahedral sites confirms the formation of spinel structure of ferrite. The lower frequency absorption band υ_2 lies around the frequency 418 cm^{-1}, and the higher absorption band υ_1 lies around the frequency 594 cm^{-1} which are due to the stretching vibration of Fe^{+3}- O^{-2} bonds at both octahedral and tetrahedral sites, respectively. A weak absorption band appeared near 338 cm^{-1}, and assigned υ_3 is due to the vibration of the divalent metal oxygen bond $Me\text{-}O^{2-}$. The lower frequency absorption band υ_2 shifts to higher frequency as Zr content increases, whereas the higher frequency band υ_1 shifts to lower frequency.

The calculated values of force constant for both tetrahedral and octahedral sites are shown in Table 2 where the force constant of the bond $Fe^{3+}\text{–}O^{2-}$ was calculated from the formula $F = 4\pi^2\gamma^2c^2m$, where m is the reduced mass. The force constant decreases for both A and B sites, which means that the electronic distribution of $Fe^{3+}O^{2-}$ bond is affected by the addition of Zr, i.e., the intermolecular character of the given ferrite was affected by the presence of Zr.

3.4 DC resistivity of the Ferrite Samples:

The DC resistivity as a function in reciprocal temperature $\frac{1000}{T}$ k^{-1} for $Cu_{0.4}Zn_{0.6+y}Zr_yFe_{2-2y}O_4$ where ($y = 0.05$ and 0.1) is shown in Fig. 6. The resistivity decreases linearly with increasing temperature within the given range of temperature 300–666 K for all samples. The decrease in DC resistivity is
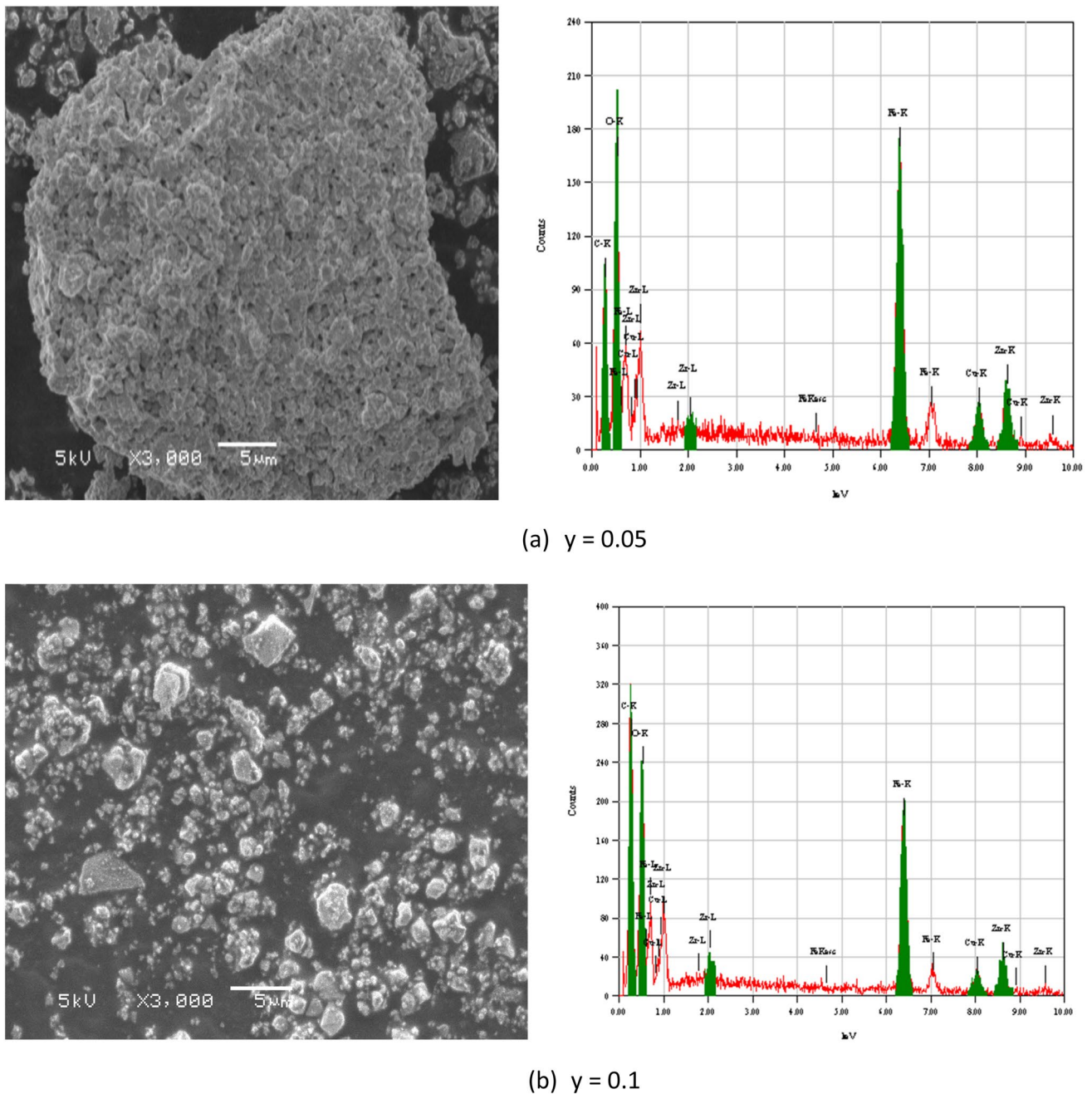
(a) y = 0.05

(b) y = 0.1

Fig. 4 SEM micrograph of $Cu_{0.4}Zn_{0.6+y}Zr_yFe_{2-2y}O_4$ ferrite doped with Zr ions with mole content ($y = 0.05$ and 0.1)

explained by the thermally activated mobility of the bound charge carriers that are hopping between Fe^{3+} and Fe^{2+}. The value of DC resistivity was found to increase with increasing Zr content as given in Table 3. The presence of Zr ions retards the hopping process between Fe^{3+} and Fe^{2+} and decreases the conductivity. The DC resistivity versus $\frac{1000}{T}$ plot consists of three regions and two break points. This second break point T_2 was shifted to lower temperature by increasing Zr content.

The first region in the DC resistivity plot may be due to the humidity, and the first break point for all samples was near 100 °C. The second and third regions were belonging to the order ferrimagnetic and the disorder paramagnetic region which are separated by the second break point. The activation energy for ferromagnetic region E_f and for paramagnetic region E_p is given in Table 3.

The lower value of activation energy in ferrimagnetic region (less than 1 eV) suggests the presence of hopping

Fig. 5 FTIR spectra of $Cu_{0.4}Zn_{0.6+y}Zr_yFe_{2-2y}O_4$ where ($y=0.05$ and 0.1)

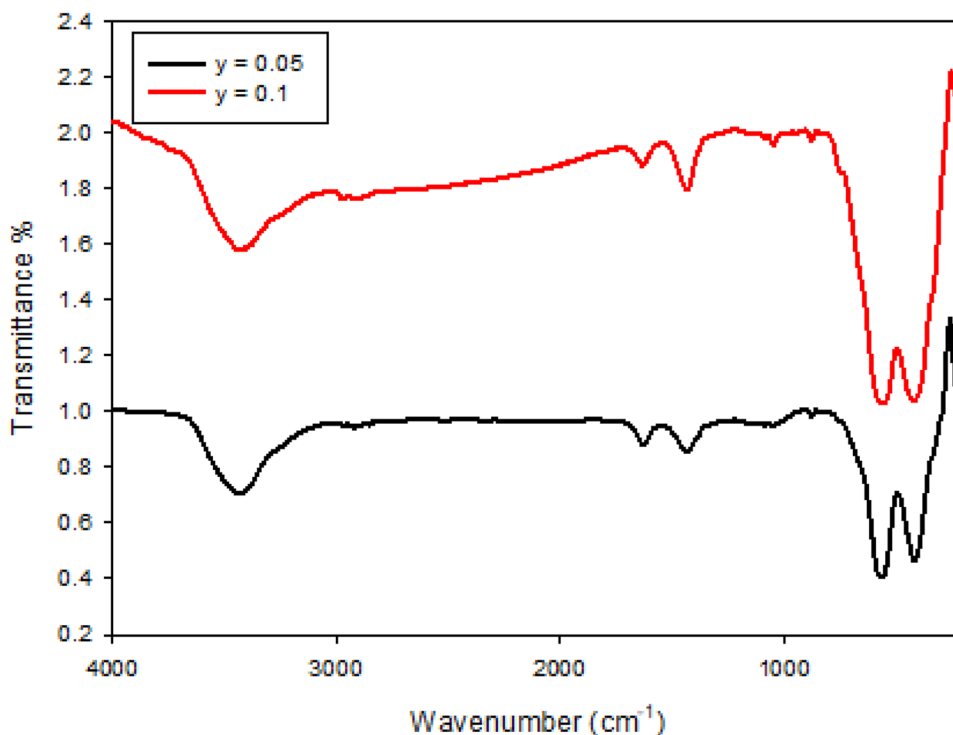**Table 2** Force constant for both tetrahedral and octahedral sites of $Cu_{0.4}Zn_{0.6+y}Zr_yFe_{2-2y}O_4$ where ($y=0.05$ and 0.1)

y	F_{Tetra} (dyne/cm)	F_{Octa} (dyne/cm)
0.05	76×10^3	40×10^3
0.1	78×10^3	41×10^3

conduction mechanism in our ferrite system. The value of activation energy for ferrimagnetic and paramagnetic regions has high values compared with previous work for the same ferrite system prepared by ceramic method [51], which means there is a high influence of the preparation method on the electrical properties of the ferrite system.

Fig. 6 The variation of DC conductivity as a function of reciprocal temperature for $y=0.05$ and 0.1
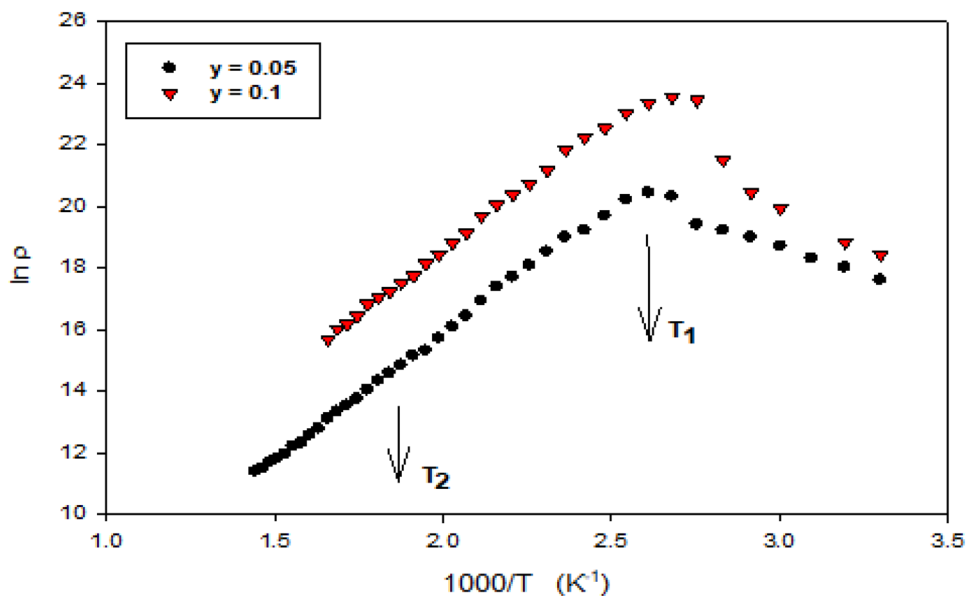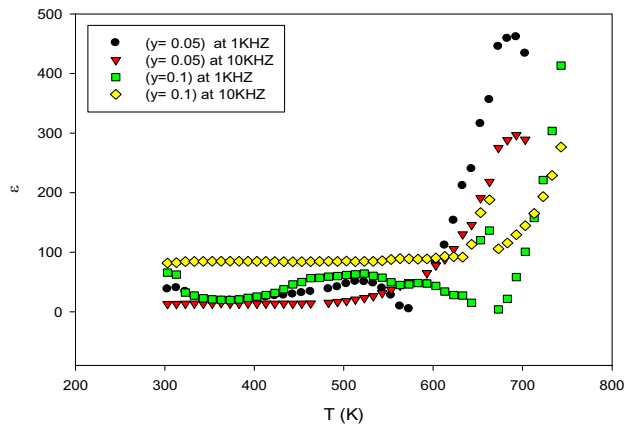
Table 3 The activation energy E_f and E_p for $y = 0.05$ and 0.1

y	Lnρ	T_2 (K)	E_p (eV)	E_f (eV)
0.05	20.4	493	0.67	0.63
0.1	23.5	433	0.72	0.59

Fig. 7 The variation of dielectric constant as a function of temperature for $y = 0.05$ and 0.1

3.5 Dielectric properties of nanoferrites

The real part of dielectric constant as a function of temperature at different frequencies 1KHZ and 10KHZ is shown in Fig. 7. The dielectric properties in ferrite are enhanced from four types of polarization interfacial, dipolar, atomic, and electronic which are predominant at low frequencies. The rapid increase in dielectric constant is due to interfacial and dipolar polarization which are strongly temperature dependent. The accumulation of charges on the grain boundary is the main reason for the presence of the interfacial polarization and the increase in dielectric constant (ε).

The electronic exchange interaction between Fe^{2+} and Fe^{3+} gives a local displacement of electrons in the direction of the external applied field which increase both dielectric constant and conductivity. So, we can say that the mechanism of polarization is similar to the mechanism of conduction in ferrite [52]. The electronic exchange interaction is the origin of electronic polarizations enhanced by increasing temperature where the mobility of hopping electrons is thermally activated and causes the increase in dielectric constant. The dielectric constant decreases by increasing Zr content and frequency as shown in Fig. 7. It was found that DC resistivity increases by increasing Zr content, i.e., the conductivity decreases which is associated with the decrease in dielectric constant. The accumulation of Zr^{4+} ions on the grain boundaries decreases the conductivity and the dielectric constant.

In conclusion, at two different selected frequencies 1 kHz and 10 kHz it was found that as the temperature increases, ε increases. The behavior of ε with Zr content has inverse character to that of resistivity. This behavior can be explained on the basis of assumption that a strong correlation between electrical conductivity and dielectric constant exists in ferrite.

3.6 Initial magnetic permeability

The initial magnetic permeability (μ_i) was measured versus temperature from room temperature up to 400K at fixed frequency 10 KHz for Zr= 0.05, 0.1 content which is shown in Fig. 8.

The decrease of μ_i as Zr content increases is attributed to the increase in magnetic anisotropy field according to Globus relation [53]:

$$\mu_i = \frac{M_s^2 D}{\sqrt{k}}$$

where K is anisotropy constant, D is the average grain size, and M_s is the saturation magnetization.

Hopkinson peak appears near T_C due to the presence of pure spinel phase. Due to the transformation from ferrimagnetic to paramagnetic, the permeability decreases at T_C. The fast decrease in magnetic anisotropy with temperature than M_s leads to the presence of HT. This material is strong candidate for MTT device due to the very high slope of the linear part of permeability. Also, the low value of Curie temperature and crystallite size is an important reason to use this material in hyperthermia applications.

The Curie temperature decreases by increasing Zr contents which mean that T_C for Zr = 0.1 is less than the sample 0.05. The Curie temperatures obtained from permeability are given in Table 4.

The Curie temperature was estimated from (μ_i) versus temperature axes. The slope of linear part was measured for the two samples as shown in Table 4; the higher the slope, the better the material can be used as magnetic temperature transducer device. It is very important to say that we can obtain the material with desired T_C by controlling the ratio of Zr content. The decrease in Curie temperature may be due to the presence of Zr ions which obstruct the A–B exchange interaction resulting in the decrease in net magnetization and Curie temperature.
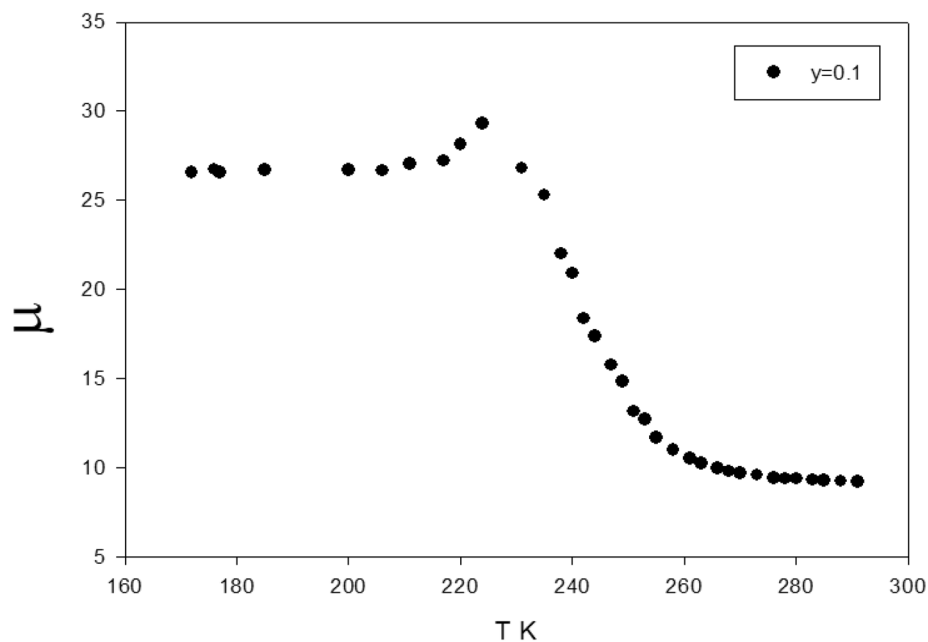
3.7 Hysteresis loop

Figure 9 shows the magnetic hysteresis loop for $Cu_{0.4}Zn_{0.6}Fe_2O_4$ doped with Zr (0.05, 0.1). The material exhibits typical magnetic hysteresis loop of soft ferrite.

Fig. 8 The variation of initial magnetic permeability (μ_i) with temperature for **a** $y = 0.05$ and **b** $y = 0.1$
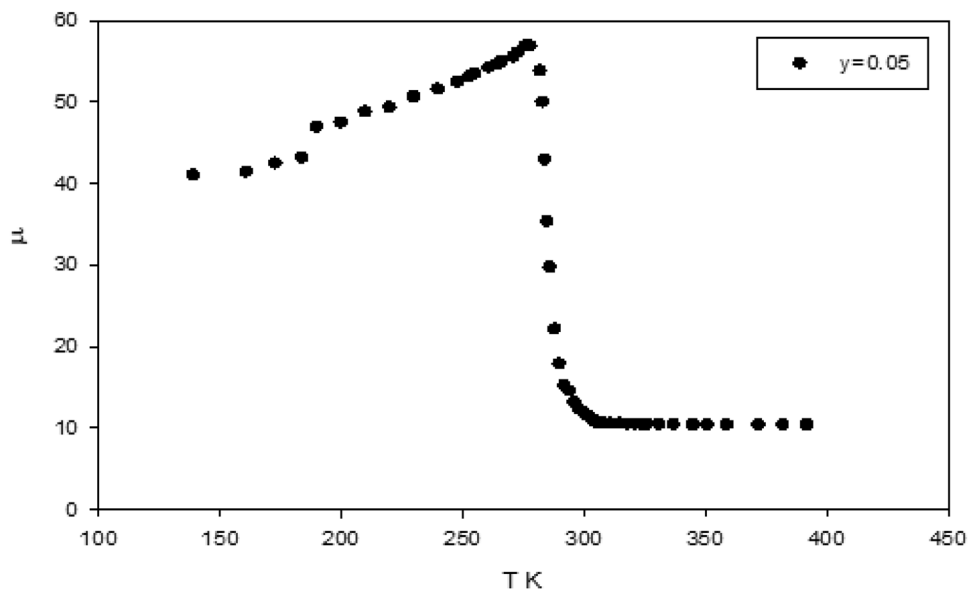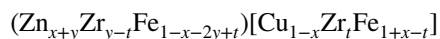

(a)

(b)

Table 4 The values of T_C (K) and rate of decrease of μ_i with $y = 0.05, 0.1$

y	T_C (K)	Rate of decrease μ_i (K^{-1})	
0.05	318	− 7.02	− 6.83
0.1	270	− 0.62	0.58

From Neel's theory, μ_{th} is given by $\mu_{th} = |M| = |M_B| - |M_A|$. The μ_{th} depends on the cation distribution among A and B sites. The general formula for proposed cation distribution is given by:
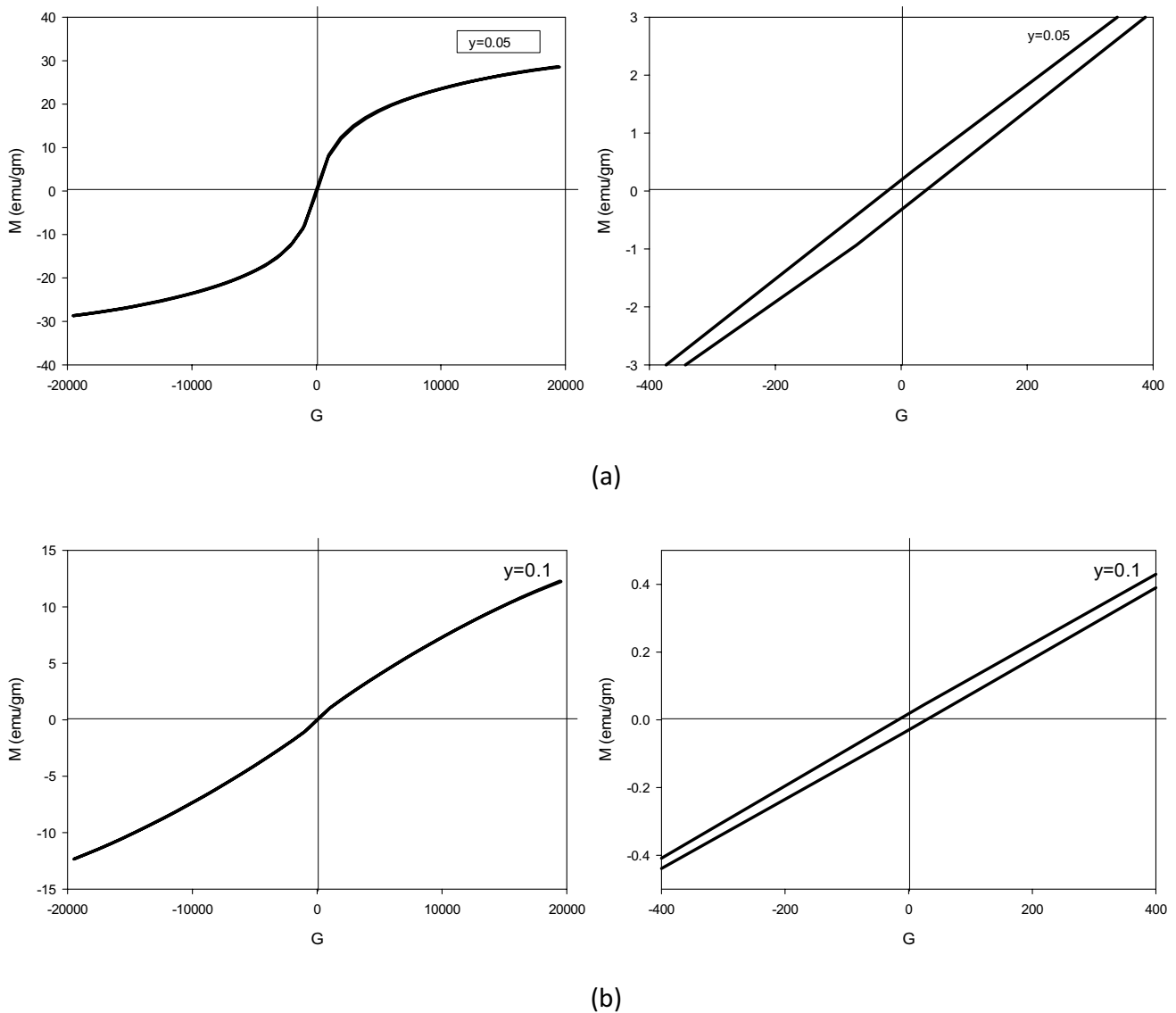
$$(Zn_{x+y}Zr_{y-t}Fe_{1-x-2y+t})[Cu_{1-x}Zr_tFe_{1+x-t}]$$

(a)

(b)

Fig. 9 Magnetic hysteresis loop for Cu–Zn–Zr ferrite for **a** $y=0.05$, **b** $y=0.1$

where $t = 0.2y$ and μ_B is Bohr magneton.

To calculate μ_{th}, we will take into consideration the distribution of ions between A and B site where Zn and Zr are non-magnetic ions. The non-magnetic ions Zn^{2+} and Zr^{4+} replace Fe^{3+} and Cu^{2+} ions with high spin magnetic moment (5 μ_B) and (1.73 μ_B), respectively. This leads to the lowering of A–B exchange interaction, and consequently, the saturation magnetization decreases at high Zr content.

The experimental magnetic moment can be calculated from the relation:

$$\mu_{exp} = \frac{M_w \times M_S}{5585}$$

where M_s is the saturation magnetization obtained from hysteresis loop curve (Table 5).

Table 5 Experimental and theoretical magnetic moments for $y=0.05$, 0.1

y	Cation distribution		μ_{th} (μ_B)	μ_{exp} (μ_B)	α_{Y-K} (°)
	A-site	B-site			
0.05	$(Zn_{0.65}Zr_{0.04}Fe_{0.31})$	$[Cu_{0.4}Zr_{0.01}Fe_{1.59}]$	6.84	1.24	71.1
0.1	$(Cu_{0.4}Zn_{0.7}Zr_{0.1}Fe_{1.8}O_4)$	$[Zn_{0.7}Zr_{0.08}Fe_{0.22}]$	6.99	0.54	78.9

The non-coincidence of μ_{th} and μ_{exp} means that the ionic magnetic moment at B site is not parallel to each other, but it makes some canting with an angle called Yafet–Kittel angle using the formula [54]:

$$\mu_{\text{exp}} = \mu_{\text{B}} \cos \alpha_{Y-K} - \mu_{\text{A}}$$

where α_{Y-K} is the Yafet–Kittel angle. The values of $\mu_{\text{th}}, \mu_{\text{exp}}$, and α_{Y-K} for the samples were measured at room temperature and are given in Table 6.

A correlation between D and M_{s} for both samples $y = 0.05$ and 0.1 is shown in Table 6. It was observed that the average crystallite size increases with increasing Zr content. This variation has an opposite relation for the saturation magnetization. Similar results have been reported by [55].

The decrease in the B–B exchange interaction at high Zr content ($y = 0.1$) leads to the decrease of M_{s}, due to the presence of large radius Zr^{4+} ion. As the Zr content increases, the material transfer to a superparamagnetic state and the coercivity become a very small value.

According to Brown's relation [53], the decrease in H_{c} with the increase in Zr content is due to the decrease in magnetic crystalline anisotropy [56] as shown in Table 6:

$$H_{\text{c}} \geq \frac{2k_i}{\mu_{\text{o}} M_{\text{s}}}$$

where k is the magnetic anisotropy and μ_{o} is the universal constant of permeability for free space.

When the permeability decreases, the coercivity still decreases also which indicates that the anisotropy constant K is the dominant factor. The same behavior was observed in the previous study [57, 58].

Table 6 The variation of crystalline size, saturation magnetization, and coercivity for both ratios for $y = 0.05, 0.1$

Y	M_{s} (emu/g)	D (nm)	H_{c} (G)	Permeability at room temperature
0.05	31	20.8	40	42
0.1	15	27.6	36	27

3.8 Hyperthermia heating

Magnetic particles reach the cancer cell through direct injection [59]. Due to hysteresis of ferrimagnetic material, the temperature increases within 42–46 °C and destroys the tumor cells. The heat generation is controlled by the magnetic properties of the material. We can observe magnetic loss due to the changes in the direction of magnetic domains. To optimize the transformation of magnetic energy to heat, the material is preferred to have no superparamagnetic behavior and have a small particle in the range of nanosize to increase the production of heat within tumor tissue.

The multi-domain structures permit some domains to extend in the direction of external magnetic field, and the other shrinks, i.e., there is a magnetic domain wall displacement. The work performed is given by:

$$E_{\text{ng}} = \int_0^M \mu_0 H_{\text{ext}} \, dM$$

This is associated by losses, so the material produces heat under the effect of AC magnetic field. Another factor is the rotation of magnetic moment around the magnetic field which then relaxes back to its original orientation. The friction arising from magnetic moment rotation produces heat. This is predominant in tiny size particles. When the loop area is large, it will generate sufficient work to move the magnetic domains.

Finally, SPL strongly depends on M_{s} as well as the volume fraction and particle size and shape of the particles. High M_{s} is required to increase the temperature of the tumor cell. The main goals of the HT are to satisfy three conditions: (1) The raise in temperature is above 42 °C which should be maintained for a certain time, (2) the temperature 41 °C is the minimum temperature for hyperthermia and (3) the temperature of surrounding tissues is kept below 45 °C.

Therefore, the maximum temperature and the time needed to reach critical temperature 42 °C in addition to SPL value are considered the main factor during introduction a new nanomaterials for hyperthermia applications.

Hysteresis areas are entirely dependent upon particle size, magnetic anisotropy, and domain wall movement. VSM hysteresis loop at 400 Oe is more suitable in clinical laboratory. For multi-domain structure, the coercivity decreases
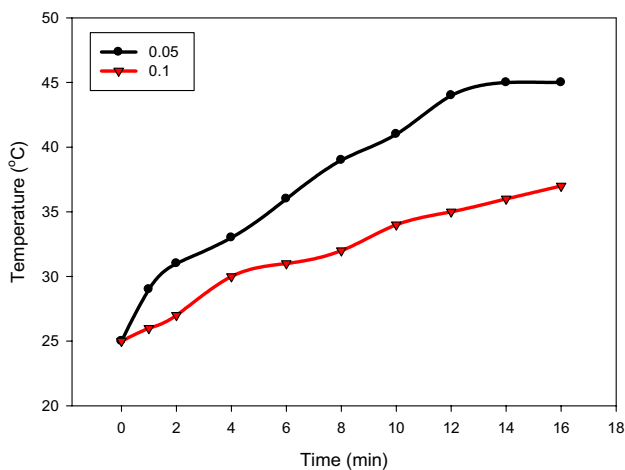
Table 7 Crystallite size, $\frac{m_{\text{sample}}}{m_{\text{water}}}$, initial slope $\left(\frac{\Delta T}{\Delta t}\right)$, maximum temperature, concentration, and specific power loss (SPL) for different Zr contents

Zr content	Crystallite size (nm)	$\frac{m_{\text{sample}}}{m_{\text{water}}}$	Initial slope $\left(\frac{\Delta T}{\Delta t}\right)$	Maximum temperature	Concentration $\left(\frac{2\,\text{gram}}{300\,\text{mL water}}\right)$	SPL W/g
0.05	20.8	66.1	0.065	45 °C	0.15	23.5
0.1	27.6	66.1	0.025	Not achieved	0.15	7.1

Fig. 10 Heating curve of the samples $y = 0.05$ and $y = 0.1$

with the increase in crystallite size because the domain wall can rotate easily along the magnetic field, whereas in single domain structure the coercivity increases with increase in the crystallite size. Calorimetric value increases with the increase in coercivity and hysteresis area which indicate the energy loss in a complete cycle of magnetization and demagnetization. As given in Table 7, it was noticed that as the coercivity and the area of the hysteresis loop increase, the energy loss in a complete cycle increases which is considered as an important parameter in the magnetic heat generation.

Heating curve of the samples $y = 0.05$ and $y = 0.1$ is shown in Fig. 10. For different Zr contents, the curve has two regions, the first one through 1–2 min with sharp increase in temperature which is due to the alignment of magnetic moment under AC magnetic field and the second region related to the hysteresis loss due to ferrimagnetic behavior of the samples. The heating process is a combination of hysteresis loss, Brownian relaxation, and Neel relaxation. The heating rate was increased by decreasing Zr content.

These results are in the range of SPL reported previously for $Zn_{0.5}Ca_{0.5}Fe_2O_4$ [60], $Mg_{0.4}Zn_{0.1}Fe_2O_4$ [42], $Mg_{0.7}Zn_{0.3}Fe_2O_4$ [42], and $MgFe_2O_4$ [61], where the values of SAR were 14.8, 10.29, 18.73, and 19(W/g), respectively.

4 Conclusion and summary

The X-ray diffraction patterns for copper ferrite samples with $x = (0.6)$ and $y = (0.05, 0.1)$ showed all the diffraction peaks were indexed which are referred a face-centered single spinel cubic phase with a face-centered cubic (fcc) structure. The crystallite size deduced from TEM was near to that calculated from XRD. As noticed from the IR absorption spectra, the broadening of the band decreases by increasing

Zr content. The fast decrease in initial permeability μ_i at T_c is a good reason to be a very strong candidate for magnetic switch devices. The material exhibits typical magnetic hysteresis loop of soft ferrite which indicates that it is magnetically ordered at low Zr content. At higher Zr content, the material behaves as superparamagnetic material without any saturation M_s and very small coercivity around zero. The resistivity decreases linearly with increasing temperature within the given range of temperature 666 k for all samples. The dielectric constant decreases by increasing Zr content. The heating rate was increased by decreasing Zr content. Also, at $x = 0.05$ there is stability in the heating curve and it does not exist at $x = 0.1$. The relation between crystallite size and SPL was also studied.

References

1. R.M. Patil, N.D. Thorat, P.B. Shete, S.V. Otari, B.M. Tiwale, S.H. Pawar, Mater. Sci. Eng. C **59**, 702 (2016)
2. A.U. Rashid, P. Southern, J.A. Darr, S. Awan, S. Manzoor, J. Magn. Magn. Mater. **344**, 134 (2013)
3. J. Huanga, M. Chena, W. Kuoa, Y. Suna, F. Lin, Ceram. Int. **41**, 2399 (2015)
4. M. Mishra, A. Roy, A. Garg, R. Gupta, S. Mukherjee, J. Alloys Compd. **721**, 593 (2017)
5. L. Li, X. Zhong, R. Wang, X. Tu, J. Magn. Magn. Mater. **435**, 58 (2017)
6. A.M. EL-Rafei, A.S. El-Kalliny, T.A. Gad-Allah, J. Magn. Magn. Mater. **428**, 92 (2017)
7. F. Ebrahimi, S.R. Bakhshi, F. Ashrafizadeh, A. Ghasemi, Mater. Res. Bull. **76**, 240 (2016)
8. Y. Bi, Y. Ren, F. Bi, T. He, J. Alloys Compd. **646**, 827 (2015)
9. Z. Song, Y. He, Appl. Surf. Sci. **420**, 911 (2017)
10. F.S. Yardımcı, M. S¸Enel, A. Baykal, Mater. Sci. Eng. C **32**, 269 (2012)
11. M. Sundararajan, L. John Kennedy, P. Nithya, J. Judith Vijaya, M. Bououdina, J. Phys. Chem. Solids **108**, 61 (2017)

12. C.S.S.R. Kumar, F. Mohammad, Adv. Drug Deliv. Rev. **63**, 789 (2011)

13. O.M. Lemine, K. Omri, M. Iglesias, V. Velasco, P. Crespo, P. de la Presa, L. El Mir, HoucineBouzid, A. Yousif, Ali Al-Hajry, J. Alloys Compd. **607**, 125 (2014)

14. M. Salavati-Niasari, F. Davar, M. Mazaheri, Polyhedron **27**, 3467–3471 (2008)

15. M. Salavati-Niasari, J. Hasanalian, H. Najafian, J. Mol. Catal. A: Chem. **209**, 209–214 (2004)

16. S. Mortazavi-Derazkola, S. Zinatloo-Ajabshir, M. Salavati-Niasari, Ceram. Int. **41**(8), 9593–9601 (2015)

17. D. Ghanbari, M. Salavati-Niasari , M. Sabet, Compos. Part B **45**, 550–555 (2013)

18. M. Salavati-Niasari, A. Sobhani, F. Davar, J. Alloys Compd. **507**, 77–83 (2010)

19. M. Salavati-Niasari, F. Davar, M.R. Loghman-Estarki, J. Alloys Compd. **494**, 199–204 (2010)

20. F. Ansaria, A. Sobhanib, M. Salavati-Niasari, J. Magn. Magn. Mater. **410**, 27–33 (2016)

21. S. Zinatloo-Ajabshira, M.S. Morassaeib, O. Amiric, M. Salavati-Niasarib, Ceram. Int. **46**, 6095–6107 (2020)

22. R. Eivazzadeh-Keihan, F. Khalili, N. Khosropour, H.A.M. Aliabadi, F. Radinekiyan, S. Sukhtezari, A. Maleki, H. Madanchi, M.R. Hamblin, M. Mahdavi, S.M.A. Haramshahi, A.E. Shalan, S. Lanceros-Méndez, ACS Appl. Mater. Interf. **13**(29), 33840−33849 (2021)

23. R. Eivazzadeh-Keihan, S. Asgharnasl, M.S. Bani, F. Radinekiyan, A. Maleki, M. Mahdavi, P. Babaniamansour, H. Bahreinizad, A.E. Shalan, S. Lanceros-Méndez, Langmuir **37**(29), 8847−8854 (2021)

24. R. Eivazzadeh-Keihan, H.A.M. Aliabadi, F. Radinekiyan, M. Sobhani, F. Khalili, A. Maleki, H. Madanchi, M. Mahdavi, A.E. Shalan, RSC Adv. **11**(29), 17914–17923 (2021)

25. M. Latorre-Esteves, A. Cortes, M. Torres-Lugo, C. Rinaldi, J Magn Magn Mater. **321**, 3061–3066 (2009)

26. H.M. Zaki, S.H. Al-Heniti, T.A. Elmosalami, J Alloy Compd. **633**, 104–114 (2015)

27. M. ManjurulHaquea, M. Huq, M.A. Hakim, Mater. Chem Phys. **112**, 580–586 (2008)

28. A. Ghasemi, A. Ashrafizadeh, A. PaesanoJr, C.F.C. Machado, S.E. Shirsath, X. Liu et al., J Magn Magn Mater. **322**, 3064–3071 (2010)

29. A. Apostolov, I. Apostolova, J. Wesselinowa, Eur. Phys. J. B **92**, 3 (2019)

30. B.T. Mai, P.B. Balakrishnan, M.J. Barthel, F. Piccardi, D. Niculaes, F. Marinaro, S. Fernandes, A. Curcio, H. Kakwere, G. Autret et al., ACS Appl. Mater. Interf. **11**, 5727–5739 (2019)

31. R. Gupta, D. Sharma, ACS Chem. Neurosci. **10**, 1157–1172 (2019)

32. M.V. Velasco, M.T. Souza, M.C. Crovace, A.J. Aparecido de Oliveira, E.D. Zanotto, Biomed Glasses **5**, 148–177 (2019)

33. C.H. Hou, S.M. Hou, Y.S. Hsueh, J. Lin, H.C. Wu, F.H. Lin, Biomaterials **30**, 3956–3960 (2009)

34. H. Wu, T. Wang, M. Bohn, F. Lin, M. Spector, Adv. Funct. Mater **20**, 67–77 (2010)

35. G. Li, D. Zhou, Y. Lin, T. Pan, G. Chen, Q. Yin, Mater. Sci. Eng. C **30**, 148–153 (2010)

36. F.M. Martin-Saavedra, E. Ruiz-Hernandez, A. Bore, D. Arcos, M. Vallet-Regi, N. Vilaboa, Acta Biomater. **6**, 4522–4531 (2010)

37. P.E. Le Renard, O. Jordan, A. Faes, A. Petri-Fink, H. Hofmann, D. Rufenacht, F. Bosman, F. Buchegger, E. Doelker, Biomaterials **31**, 691–705 (2010)

38. N. Bock, A. Riminucci, C. Dionigi, A. Russo, A. Tampieri, E. Landi, V.A. Goranov, M. Marcacci, V. Dediu, Acta Biomater. **6**, 786–796 (2010)

39. T.W. Wang, H.C. Wu, W.R. Wang, F.H. Lin, P.J. Lou, M.J. Shieh, T.H. Young, J. Biomed. Mater. Res. A **83**, 828–837 (2007)

40. H. Hirazawa, H. Aono, T. Naohara, T. Maehara, M. Sato, Y. Watanabe, J. Magn. Magn. Mater. **323**, 675 (2011)

41. V.M. Khot, A.B. Salunkhe, N.D. Thorat, M.R. Phadatare, S.H. Pawar, J. Magn. Magn. Mater. **332**, 48 (2013)

42. P. Yajaira Reyes-Rodríguez, D. Alicia Cortés-Hern´andez et al., J. Magn. &Magn.Mater.427, 268 (2017).

43. P. Liua, Z. Yaoa, J. Zhoua, Z. Yanga, L.B. Kong, J. Mater. Chem. C **4**, 9738 (2016)

44. P. Liua, V.M.H. Ngc, Z. Yaoa, J. Zhoua, Y. Leia, Z. Yanga, H. Lva, L.B. Kong, ACS Appl. Mater. Interf. **9**, 16404 (2017)

45. P. Liua, Z. Yaob, V.M.H. Ngc, J. Zhoub, L.B. Kong, Mater. Lett. **248**, 214 (2019)

46. R. Sridhar, D. Ravinder, K. Vijaya Kumar, Adv. Mater. Phys. Chem. **2**, 192–199 (2012)

47. E. Pollert, P. Veverka, M. Veverka, O. Kaman, K. Závěta, S. Vasseur et al., Preliminary chemical and physical issues. Prog. Solid State Chem. **37**, 1–14 (2009)

48. E. Rodrigues, M. Morales, S. de Medeiros, N. Suguihiro, E. Baggio-Saitovitch, J. Magn. Magn. Mater. **416**, 434–440 (2016)

49. M. Bahgat, F. Farghaly, S.A. Basir, O. Fouad, J. Mater. Process. Technol. **183**(1), 117–121 (2007)

50. H. El Moussaoui, T. Mahfoud, M.B. Ali, Z. Mahhouti, R. Masrour, M. Hamedoun, E. Hlil, A. Benyoussef, Mater. Lett. **171**, 142–145 (2016)

51. A. Tawfik, O. M. Hemeda, B. I. Salem, 90–92 (2012)

52. O.M. Hemeda, Nasser Y. Mostafa, Omar H. Abd Elkader, D. M. Hemeda, A. Tawfik, M. Mostafa, J. Mag. Mag. Mater. **394**, 96–104 (2015)

53. A. Sattar, H. El-Sayed, W. Agami, A. Ghani, Am J ApplSci **4**(2), 89–93 (2007)

54. R. Topkaya, A. Baykal, A. Demir, J. Nanopart. Res. **15**(1), 1–18 (2013)

55. Globus A, Pascard H, C.V. Le, J. Physique Colloq. 38(C1):C1-163–C161–168 (1977).

56. M.N. Ashiq, S. Saleem, M.A. Malana, J. Alloy. Compd. **486**(1), 640–644 (2009)

57. N. Yahya, M.N. Aripin, A. Salwani, A. Aziz, H. Daud, H. MohdZaid, K.P. Lim, N. Maarof, Am. J. Eng. Appl. Sci. **1**(1), 54–57 (2008)

58. Mazen S, Dawoud H. physica status solidi (a), 172(2):275–289 (1999).

59. S.F. Karkan, M. Hosseini, Y. Panahi, M. Milani, N. Zarghami, A. Akbarzadeh, Artif. Cells Nanomed. Biotechnol. **45**, 1–5 (2017)

60. R. Argentina Jasso-Terán, D. Alicia Cortés-Hernández et al., J. Magn. Magn. Mater. **427**, 241 (2017)

61. H.M. El-Sayed, I.A. Ali, A. Azzam, A.A. Sattar, J. Magn. Magn. Mater. **424**, 226 (2017)